

1

## 2 **Supplementary Information for**

### 3 **Observation of Spontaneous Ferromagnetism in a Two-Dimensional Electron System**

4 **Md. S. Hossain, M. K. Ma, K. A. V. Rosales, Y. J. Chung, L. N. Pfeiffer, K. W. West, K. W. Baldwin, and M. Shayegan**

5 **L. N. Pfeiffer**

6 **E-mail: [loren@princeton.edu](mailto:loren@princeton.edu)**

7 **or**

8 **M. Shayegan**

9 **E-mail: [shayegan@princeton.edu](mailto:shayegan@princeton.edu)**

#### 10 **This PDF file includes:**

11     Supplementary text

12     Figs. S1 to S11

13     SI References

## 14 Supporting Information Text

### 15 I. Experimental Details

16 Our material platform is an AlAs quantum well epitaxially grown via molecular beam epitaxy on a GaAs substrate. In  
17 particular, our sample contains a 21-nm-wide AlAs quantum well sandwiched by 68-nm-thick  $\text{Al}_{0.38}\text{Ga}_{0.62}$  spacer barriers.  
18 Similar to the case of GaAs, as long as the conduction band offset between the barrier and the quantum well is sufficiently  
19 large, it is possible to confine carriers in the AlAs quantum well through modulation doping (1–3). The main difference is that  
20 in AlAs the conduction band has lower energy at the X-points of the Brillouin zone instead of the  $\Gamma$ -point. Therefore, the  
21 electrons in our AlAs quantum well are confined in the X-point valleys.

22 In bulk AlAs, electrons occupy three energetically degenerate ellipsoidal (or six half ellipsoidal) conduction band valleys at  
23 the six equivalent X-points of the first Brillouin zone (2). We denote these valleys as [100], [010], and [001] with their major  
24 axes lying along the [100], [010], and [001] crystallographic directions, respectively (see Fig. S1A). The electrons in each valley  
25 possess an anisotropic Fermi surface with longitudinal and transverse effective masses of  $m_l = 1.1$  and  $m_t = 0.20$  in units of  
26 the free electron mass (2).

27 When an AlAs quantum well is formed along the [001] axis, the confinement in the growth direction splits the three-fold  
28 valley degeneracy because of the difference in the effective mass along the in-plane and out-of-plane directions. We refer to the  
29 out-of-plane valley as [001], and the in-plane valleys as [100] and [010]. At first sight, one would expect that the [001] valley  
30 should be occupied at all well-widths since it has the larger mass along the confinement direction. However, the slightly larger  
31 lattice constant of AlAs compared to GaAs causes biaxial compression in the plane of the AlAs layer, lowering the conduction  
32 band of the [100] and [010] valleys relative to the [001] valley. This causes the ground-state energies of the two types of valleys  
33 to cross at a critical quantum well width of  $\simeq 6$  nm (2). Above this well-width, the [100] and [010] valleys are occupied; this is  
34 the case for our 21-nm-wide AlAs quantum well (Fig. S1B).

35 In the absence of any additional in-plane strain, electrons in our AlAs quantum well occupy two in-plane valleys ([100] and  
36 [010]) (Fig. S1B). This two-fold valley-degeneracy can be lifted via the application of an in-plane, symmetry-breaking, strain  
37  $\Delta\varepsilon = \varepsilon_{[100]} - \varepsilon_{[010]}$ , where  $\varepsilon_{[100]}$  and  $\varepsilon_{[010]}$  are the strain values along [100] and [010] (2). The valley splitting energy is given by  
38  $E_V = \varepsilon E_2$ , where  $E_2$  is the deformation potential, which in AlAs has a band value of 5.8 eV. Positive strain pushes the energy  
39 of the [100] valley up relative to the [010] valley, causing electrons to transfer from [100] to [010], and vice versa for negative  
40 strain.

41 In Fig. S1C we show our experimental setup for applying tunable in-plane strain to the two-dimensional electron system  
42 (2DES). We glue the sample on one side of a stacked piezoelectric lead-zirconate-titanate actuator with a commercial two-part  
43 epoxy (4). Note in Fig. S1C that the sample is glued with its [100] axis along the poling direction of the piezo-actuator. The  
44 piezoelectric actuator deforms when a voltage ( $V_P$ ) is applied across its two leads and hence strains the sample glued to its  
45 top surface. Thus, we introduce nearly uniaxial, in-plane strain to our 2DES. The strain in our sample is  $3.6 \times 10^{-7}$  per Volt  
46 applied to the piezo-actuator.

47 In order to maintain sufficient strain homogeneity, we used small van der Pauw samples with typical dimensions of 1.5 mm  
48  $\times$  1.5 mm. Note that the sample edges are along the GaAs cleave directions, [110] and  $\bar{[110]}$  (see Fig. S1C). The samples are  
49 lapped and polished on the back-side down to 150  $\mu\text{m}$  in order for the strain to propagate to the 2DES (4). Electron-beam  
50 evaporated Ti-Au alloy on the back-side of the sample shields the 2DES from the electric field generated by the applied  $V_P$ ,  
51 and also serves as a back gate which we use to change the 2DES density *in situ*. Electrical contacts to the 2DES are achieved  
52 via alloying a eutectic mixture of In and Sn on the corners and the centers of the sample edges at 425  $^\circ\text{C}$  for 270 seconds.

53 Figure S2, which shows the sample's piezo-resistance at a 2DES density  $n = 2.90 \times 10^{10} \text{ cm}^{-2}$  as a function of  $V_P$  at zero  
54 magnetic field, demonstrates how we tune and monitor the valley occupancy. At  $V_P = -310$  V (point **b**), the 2DES exhibits  
55 isotropic transport, namely, the resistances measured along the [100] and [010] directions ( $R_{[100]}$  and  $R_{[010]}$ , respectively) are  
56 equal, even though the individual valleys are anisotropic. Point **b** corresponds to the case where the [100] and [010] valleys are  
57 equally occupied. We refer to this point where the two valleys are degenerate at the “balance” point; for the data shown in Fig.  
58 S2, this is achieved via applying a piezo bias of -310 V which we refer to as  $V_b$ .

59 For  $\Delta\varepsilon > 0$ , as electrons transfer from [100] valley to [010] valley,  $R_{[100]}$  decreases (black trace in Fig. S2) because the  
60 electrons in [010] valley have a small effective mass and therefore higher mobility along [100] (2). (Note that the total 2DES  
61 density remains fixed as strain is applied.) The resistance eventually saturates (point **c**), when all electrons are in the [010]  
62 valley (2, 5, 6). For  $\Delta\varepsilon < 0$ ,  $R_{[100]}$  increases and eventually saturates (e.g., point **a**), as the electrons are transferred to [100]  
63 valley which has a large mass and a low mobility along [100]. As expected, the behavior of  $R_{[010]}$  is opposite to that of  $R_{[100]}$ .

64 In our measurements, except for the data presented in Section III below, we use  $\Delta\varepsilon > 1 \times 10^{-4}$ , so that only the [010] valley  
65 is occupied. For data shown in Section III, we bias  $V_P$  so that either the two valleys are degenerate (Section III.A), or the  
66 electrons are divided unequally between the two valleys (Section III.B). To achieve this partial occupancy, we assume that the  
67 valley occupations are linearly proportional to the strain applied relative to the balance point (2). For example, point **d** in Fig.  
68 S2 corresponds to 75% of electrons occupying valley [100] and 25% valley [010]. Conversely, at point **e**, 25% of electrons occupy  
69 valley [100] and 75% occupy valley [010]. Furthermore, to obtain the data for [100] valley occupancy, presented in Section III.B,  
70 we use  $\Delta\varepsilon < -1 \times 10^{-4}$ , so that all the electrons occupy the [100] valley.

71 It is worthwhile noting that, a finite  $V_P$  is required to attain a balance point (point **b**) in our experiments (2, 5, 7). For  
72 example, for the data shown in Fig. S2,  $V_b$  is equal to -310 V. Such offset in the balance point occurs because of the cooldown-  
73 and sample-dependent residual strain originating from the difference in thermal contraction coefficients of the sample, glue and

74 the piezo-actuator during the cooling process (2, 5, 7).

75 We carried out our experiments in a  $^3\text{He}$  cryostat with a base temperature of  $T \simeq 0.30$  K. We use the back gate to tune the  
76 2DES density  $n$ , which we describe in units of  $10^{10} \text{ cm}^{-2}$  throughout the manuscript and the Supplementary Information.

77 In Fig. S3 we demonstrate our measurement setup, showing the voltage and current leads. We use two lock-in amplifiers,  
78 one for measuring the voltage ( $V_{AC}$ ) across the sample and another to measure the current ( $I_{AC}$ ) passing through the sample.  
79 Resistance is then determined from  $V_{AC}/I_{AC}$  via passing a small (1 nA) AC excitation of frequencies 3.0 Hz (for  $n > 1.80$ ) and  
80 1.7 Hz (for  $n \leq 1.80$ ). Note that a direct measurement of current is necessary, especially for low densities when the values of  
81 resistance are very large. Since the lock-in amplifier has a finite input impedance, which is about 10 M $\Omega$  for our setup, it causes  
82 a portion of the current to flow through the lock-in amplifier to the ground instead of passing through the sample. Therefore,  
83 one has to measure the current that flows through the sample directly to obtain an accurate measure of resistance.

## 84 II. Resistance vs. $B_{||}$ near the Metal-Insulator Transition

85 As shown in Fig. 3A of the main text, we observe a change from metallic to insulating transport at a density  $n \simeq 3.2$ . In this  
86 Section, we discuss magnetotransport data as a function of the parallel magnetic field  $B_{||}$  near this metal-insulator transition  
87 (MIT).

88 In Fig. S4, we show  $R_{[100]}$  vs.  $B_{||}$  data, similar to the data in Fig. 1C of the main text, including here the traces for a few  
89 more densities near the MIT. As we lower the 2DES density, starting from  $n \simeq 3.60$ , we observe a glimpse of an additional  
90 feature at very low  $B_{||}$ , marked with blue arrows in Fig. S4. It becomes more prominent as we approach the MIT at  $n \simeq 3.20$ .  
91 The additional feature is manifested by a sudden rise in magnetoresistance slope at very low  $B_{||}$ . The slope abruptly decreases  
92 above a certain magnetic field (marked by the blue arrows in Fig. S4), and  $R_{[100]}$  increases nearly linearly with  $B_{||}$ , eventually  
93 saturating once  $B_{||} = B_M$  is reached (see red arrows in Fig. S4). This feature at a very small  $B_{||}$  may imply another transition  
94 besides the spin transition at  $B_M$ . While we do not know its origin, it is very intriguing that this feature only exists in a  
95 narrow density range near the MIT ( $n \simeq 3.2$ ). We surmise that there might be a correlation between the appearance of the  
96 feature and the MIT.

## 97 III. Role of the Valley Degree of Freedom in the Spin Polarization of the 2D Electron System

98 In the main text, we mostly focused on the spin polarization when only one valley is occupied and briefly discussed the  
99 ferromagnetic transition as a function of valley occupancy. In this Section, we elaborate on the spin polarization of our 2DES  
100 when the electrons occupy two in-plane valleys, [100] and [010].

101 **III. A. Comparison Between Valley-Polarized and Valley-Degenerate 2D Electron System.** This subsection delineates a compara-  
102 tive study of the spin polarization and the ferromagnetic transition between the valley polarized (e.g., point **c** in Fig. S2) and  
103 valley degenerate (e.g., point **b** in Fig. S2) 2DESs.

104 In Figs. 4A-C of the main text, we presented the spin polarization of a valley degenerate 2DES. Here, in Fig. S5 we show  
105  $B_M$  and spin susceptibility data for the single-valley and valley-degenerate cases together in the same plot. It is clear from  
106 Fig. S5 that the critical density for the ferromagnetic transition in a valley-degenerate 2DES ( $n_{c(2V)}$ ) is smaller than that  
107 of a single-valley 2DES ( $n_{c(1V)}$ ). This finding of smaller critical density for full magnetization in a valley-degenerate 2DES  
108 is consistent with previous measurements (8–10) and theoretical calculations (11) concluding that the enhancement of the  
109 spin susceptibility, at a given density, is smaller for a two-valley system compared to a single-valley one. A possible way to  
110 understand this phenomenon is that the additional valley degree of freedom modifies the inter-valley exchange interaction, which  
111 also influences the spin exchange interaction, and leads to a change in the onset density of the spontaneous ferromagnetism.

112 **III.B. Spin Polarization of the 2D Electron System with Unequally Occupied Valleys.** As seen in Section III.A, the valley-  
113 degenerate 2DES requires a smaller density than the single-valley 2DES to exhibit the ferromagnetic transition. In this  
114 subsection, we elaborate on the evolution of  $B_M$  as we tune the valley occupancy, from a single-valley case to a valley-degenerate  
115 case. How we achieve this partial valley occupancy is discussed in Section I (Fig. S2).

116 In Figs. S6A-E, we plot resistance vs.  $B_{||}$  data as a function of valley occupancy, taken at five different densities. It is  
117 clear for all the densities that the magnetic field required to magnetize the system, i.e.  $B_M$ , is the largest when the valleys  
118 are degenerate. As we lift the degeneracy and move towards valley polarization,  $B_M$  starts to drop and eventually attains its  
119 smallest value when the electrons are completely valley polarized. This is again true for all the densities, as seen in Figs. S6A-E  
120 and summarized in Fig. S6F. This means that the spin susceptibility is maximum when the 2DES is valley-polarized and  
121 minimum when the valleys are degenerate, for a given density. Thanks to this interplay between the spin and valley degrees of  
122 freedom, it is possible to control the onset of the ferromagnetic transition via tuning the valley occupancy.

## 123 IV. Comparing the Resistance Values at Zero and Above Magnetizing Field Near the Spin Polarization Transition

124 Here we address an important question: At  $n_c = 2.00$ , where the 2DES makes a transition to a fully-spin-polarized state, what  
125 is the value of its resistance, and how does this value compare with the resistance at slightly higher densities (just above the  
126 transition), say, at  $n = 2.10$ ? More importantly, is the resistance value at  $n_c = 2.00$ , which is constant and independent of  $B_{||}$ ,  
127 close to the saturation value of the resistance at  $n = 2.10$  at high  $B_{||}$ , above  $B_M$ ? A positive answer would be consistent with  
128 our conjecture that the 2DES is fully spin polarized at  $n = 2.00$  without the application of any magnetic field.

129 To address this point, we show in Fig. S7 resistance ( $R_{[100]}$ ) values at  $B_{||} = 0$  and 3 T as a function of density. In the  
 130 density range of Fig. S7 data, the 2DES becomes fully spin polarized once  $B_{||}$  reaches 3 T (see Fig. 1C). We find that  $R_{[100]}$   
 131 at 3 T (green data points) is larger than its value at  $B_{||} = 0$  T (blue data points) by about a factor of two. As the density is  
 132 lowered to  $n_c = 2.00$ ,  $R_{[100]}$  becomes independent of  $B_{||}$ . Importantly, it is clear in Fig. S7 that the value of  $R_{[100]}$  at  $n_c = 2.00$   
 133 is close to the saturated value of  $R_{[100]}$  at  $B_{||} = 3$  T at  $n = 2.10$ . Furthermore, as discussed in the main text, near the full spin  
 134 polarization transition, there is hysteresis in  $R_{[100]}$  vs.  $B_{||}$  when the magnetic field sweep direction is reversed. The hysteresis  
 135 leads to a shift in the minimum polarization, i.e. minimum resistance, to a finite  $B_{||}$ ; see the inset to Fig. S7. In Fig. S7 we  
 136 also show the resistance values at the  $R_{[100]}$  minima using open symbols. These points further elucidate the large increase in  
 137 resistance at  $B = 0$  from  $n = 2.10$  to 2.00. This observation indicates that the resistance approaches the expected high field  
 138 value at  $n_c = 2.00$ , rather than staying near the value expected for an unpolarized 2DES at  $n \geq 2.10$ . This is consistent with  
 139 our conclusion that the 2DES is fully spin polarized at  $n_c = 2.00$  at  $B_{||} = 0$ , just as it is at  $n = 2.10$  at  $B_{||} = 3$  T.

140 For the case where the electrons occupy two valleys, the evolution of  $R_{[100]}$  as a function of density also corroborates our  
 141 conclusion of full spin polarization when  $R_{[100]}$  becomes independent of  $B_{||}$ . Figure S8 captures  $R_{[100]}$  values at  $B_{||} = 0$  and 3  
 142 T as a function of density. Similar to Fig. S7, here green and blue data points denote the resistance values at  $B_{||} = 0$  and 3  
 143 T, respectively; see Fig. 4A of the main text for  $R_{[100]}$  vs.  $B_{||}$  traces. At  $n = 1.40$ , where  $B_M$  vanishes, the value of  $R_{[100]}$  at  $B = 0$   
 144 is close to the high-field value of  $R_{[100]}$  at  $n = 1.50$ . This trend strengthens our conclusion that the valley-degenerate 2DES is  
 145 fully spin polarized at  $n = 1.40$  at  $B_{||} = 0$ , and the validity of associating  $B_{||}$ -independence of resistance to ferromagnetism.

## 146 V. Measurements of Differential Resistance as a Function of DC Bias

147 Measurements of sample response as a function of applied DC bias provide information on the  $I$ - $V$  characteristics of the  
 148 sample. We use such measurements to probe the pinned Wigner solid phase as shown in Fig. 3B of the main text. For these  
 149 measurements, we use a setup shown in Fig. S9. The DC input is taken from the lock-in amplifier and the DC current that flows  
 150 through the sample is obtained via measuring the voltage drop across a known series resistance (1 k $\Omega$ ) using a high-precision  
 151 DC voltmeter. On the other hand, a small AC signal (0.5 nA, 1.7 Hz) is used to extract the differential resistance directly from  
 152 the lock-in amplifier. Note that, to measure  $V_{AC}$  and  $I_{AC}$ , a scheme similar to Fig. S3 is used where we measure  $I_{AC}$  using a  
 153 separate lock-in amplifier; this enables us to measure large values of differential resistances ( $dV/dI$ ) (see Fig. S10).

## 154 VI. Density Dependence of the Pinned Wigner Solid

155 In Fig. 3B of the main text, we showed the density dependence of  $dV/dI$  as a function of applied DC bias current, taken at  
 156 different densities. The data show the onset density for the non-linear  $I$ - $V$  characteristic, which we interpret to signal the  
 157 formation of a pinned Wigner solid. In this Section, we elaborate on the density dependence of the voltage bias threshold of  
 158 the non-linear  $dV/dI$ .

159 By performing integration over our  $dV/dI$  vs.  $I_{DC}$  data, we can obtain the voltage drop along the direction of the current  
 160 passing through the sample. In Figs. S10A, B, we plot this voltage drop as a function of  $I_{DC}$ . The plots exhibit a vanishing  
 161 non-linearity as the density is raised to  $n > 1.70$ .

162 It turns out that presenting our  $dV/dI$  data as a function of the voltage drop reveals important information. Figures S10C,  
 163 D show such data. As seen in Figs. S10C, D,  $dV/dI$  decreases rather sharply above a certain threshold voltage, i.e. electric  
 164 field; that is required to depin the Wigner solid. Intriguingly, this threshold voltage depends strongly on the electron density.  
 165 At very low densities, this depinning voltage is very large. However, it drops quite abruptly as we raise the density (Fig. S10D).  
 166 And, similar to the  $dV/dI$  vs.  $I_{DC}$  data in Fig. 3B,  $dV/dI$  vs.  $V$  traces become linear and nearly flat above  $n = 1.70$  (Fig.  
 167 S10D), the density which we associate with the transition between a liquid and a pinned Wigner solid.

## 168 VII. Temperature Dependence of the Non-Linear $I$ - $V$ and the Melting of the Wigner Solid

169 In this Section, we elaborate on the temperature dependence of  $dV/dI$  as a function of electron density. We interpret the  
 170 disappearance of the non-linear DC response above a critical temperature  $T_c$  to signal the thermal melting of the Wigner solid.

171 We show in Fig. S11  $dV/dI$  data as a function of temperature for five different densities. As seen in Fig. S11A,  $T_c$  at  
 172  $n = 1.20$  appears to be between 0.95 K and 1.00 K. As we raise the density,  $T_c$  seems to decrease slightly. For example, at  
 173  $n = 1.50$ , the non-linearity disappears at  $T = 0.92$  K. As we further raise the density and approach the density ( $n = 1.80$ )  
 174 above which the Wigner solid disappears (signaled from the disappearance of the non-linear  $I$ - $V$ ),  $T_c$  drops rapidly (see Fig.  
 175 S11E). For instance, at  $n = 1.70$ , the non-linearity in the  $dV/dI$  data disappears between  $T = 0.42$  K and 0.48 K (Fig. S11E),  
 176 much lower than the range 0.81 to 0.92 K where the non-linearity disappears at  $n = 1.50$  (Fig. S11).

## 177 VIII. Applicability of the Mermin Wagner Theorem?

178 In a seminal paper in 1966, Mermin and Wagner (MW) theoretically showed that, at any non-zero temperature, there can  
 179 be no ferromagnetism in one or two dimensions (12). The model MW use is the isotropic Heisenberg spin system with  
 180 finite-range exchange interaction, and their conclusion is based on theoretically demonstrating that spin-fluctuations destabilize  
 181 ferromagnetic (as well as anti-ferromagnetic) order in an infinitely-large 2D system. We would like to note that the MW  
 182 theorem might not be directly applicable to our experiments because:

183 (i) Our sample has a finite size (about 1.5 mm by 1.5 mm).

184 (ii) The 2DES in our sample has a finite (non-zero) electron layer thickness; this may help stabilize the ferromagnetic order.  
185 (iii) The 2D electrons in our AIAs sample occupy a valley with an anisotropic effective mass. Electron-electron interaction  
186 in an anisotropic system is different from an isotropic system, possibly allowing a violation of the MW theorem.

## 187 IX. Related Systems/Phenomena

188 As discussed in the main text, spin-polarization and metal-insulator transition in dilute 2D carrier systems have been subjects  
189 of great interest. However, as described in the main text, prior to our work described here, there have been no clear reports of  
190 itinerant ferromagnetism in a system of electrons in the limit of zero magnetic field. In this Section, we discuss several plausible  
191 candidates that might exhibit such a phenomenon. We also briefly discuss the investigations on spontaneous magnetization in  
192 two exotic systems.

193 **IX.A. Spin Polarization of 2D Electrons in Other Semiconductor Systems.** A large  $r_s$  that is required to observe a full magne-  
194 tization can possibly be obtained in other 2D systems. One such candidate for the experimental realization of spontaneous  
195 ferromagnetism is the 2DES at the MgZnO/ZnO interface (13, 14). Similar to our AIAs quantum wells, this system also hosts  
196 a large-mass, high-quality 2DES (13, 14), and can potentially be a platform to exhibit a ferromagnetic transition at zero  
197 magnetic field.

198 Another emerging material platform is the 2DES in a monolayer of MoS<sub>2</sub>. In the MoS<sub>2</sub> 2DES,  $r_s$  is large thanks to the large  
199 electron effective mass and small dielectric constant. However, MoS<sub>2</sub> has a complex energy band structure: the 2D electrons  
200 occupy multiple conduction-band valleys, and also there is a strong spin-orbit interaction, linking the spin and valley degrees  
201 of freedom (15). (This is very different from our AIAs 2DES where we can control the spin and valley degrees of freedom  
202 individually because there is no spin-valley locking or spin-orbit interaction.) Recent studies by Roch *et al.* (15, 16) report the  
203 observation of spin-polarized electrons at electron densities  $n \simeq 5 \times 10^{12} \text{ cm}^{-2}$ , which correspond to  $r_s \simeq 5$ . A subsequent  
204 theoretical work (17) supports such a ferromagnetic phase. In this theory, the ferromagnetism arises from non-analyticities  
205 which go beyond Fermi liquid theory. Note that the data in Refs. (15, 16) were taken in a very large magnetic field (9.0 T). It  
206 is also worth noting that magnetotransport data in nominally similar samples at comparable densities and magnetic fields (18)  
207 exhibit Shubnikov-de Haas oscillations which do not appear to be consistent with a fully-polarized system.

208 **IX.B. Ferromagnetism in Exotic Fermionic Systems.** Itinerant ferromagnetism has been observed in three-dimensional systems  
209 (19, 20). However, these observations were made in ultra-cold atoms, not in a system of electrons.

210 There is also a very recent study demonstrating an interaction-driven spin polarization of composite fermions (21). Composite  
211 fermions are quasiparticles formed in finite magnetic fields, at and near the half-filling of the lowest Landau level. Experiments  
212 performed in a GaAs 2DES show that the composite fermions are fully spin polarized at high electron densities thanks to a  
213 large Zeeman energy. However, as the density is lowered, the composite fermions lose their full magnetization and become  
214 partially spin polarized. This is expected and stems from a relative reduction of the Zeeman energy compared to the Coulomb  
215 energy (22). Surprisingly, however, as the density is further reduced, composite fermions make a sudden transition back to a  
216 fully-magnetized state. This spontaneous magnetization of composite fermions is reminiscent of the Bloch ferromagnetism.  
217 Moreover, the theoretical calculations based on quantum Monte Carlo analysis presented in Ref. (21) suggest that the full  
218 magnetization of the composite fermions at very low densities occurs because of an enhanced interaction between composite  
219 fermions due to Landau level mixing, which is significant at small  $n$ . It is worth emphasizing that, while the interaction-driven  
220 spin polarization is thus seen in composite fermion quasiparticles formed in a finite perpendicular magnetic field, spontaneous  
221 ferromagnetism for electrons at *zero magnetic field*, has remained elusive prior to our work on AIAs 2DES presented in this  
222 manuscript.

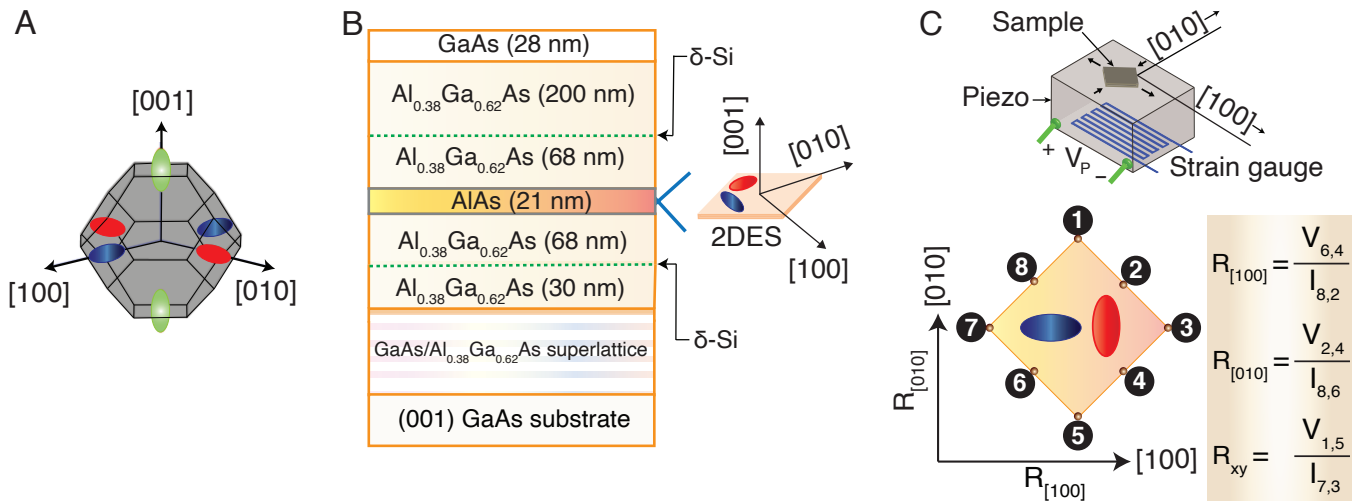


**Fig. S1.** (A) First Brillouin zone and constant energy surfaces of the lowest-energy bands for bulk AlAs, showing the [100], [010], and [001] valleys; [100], [010], and [001] refer to the crystallographic directions. (B) Structure of our AlAs 2DES grown on a GaAs substrate. The growth direction is [001]. The AlAs layer is under compressive biaxial strain because of the slightly larger lattice constant of AlAs relative to GaAs. This strain results in the occupancy of [100] and [010] valleys only. (C) Schematic of the experimental setup for applying in-plane strain ( $\Delta\varepsilon$ ). The sample is glued on top of a piezo-actuator, and strain is introduced when a bias voltage ( $V_P$ ) is applied to the actuator's leads. The sample geometry, including the orientation of the two occupied valleys ([100] and [010]), are also shown. Contacts to the sample are denoted by 1-8. For  $R_{[100]}$ , we pass current from contact 8 to 2 and measure the voltage between contacts 6 and 4. For  $R_{[010]}$ , the current is passed from contact 8 to 6 and we measure the voltage between contacts 2 and 4. On the other hand, for  $R_{xy}$ , we pass current from contact 7 to 3 and measure the voltage across contacts 1 and 5.

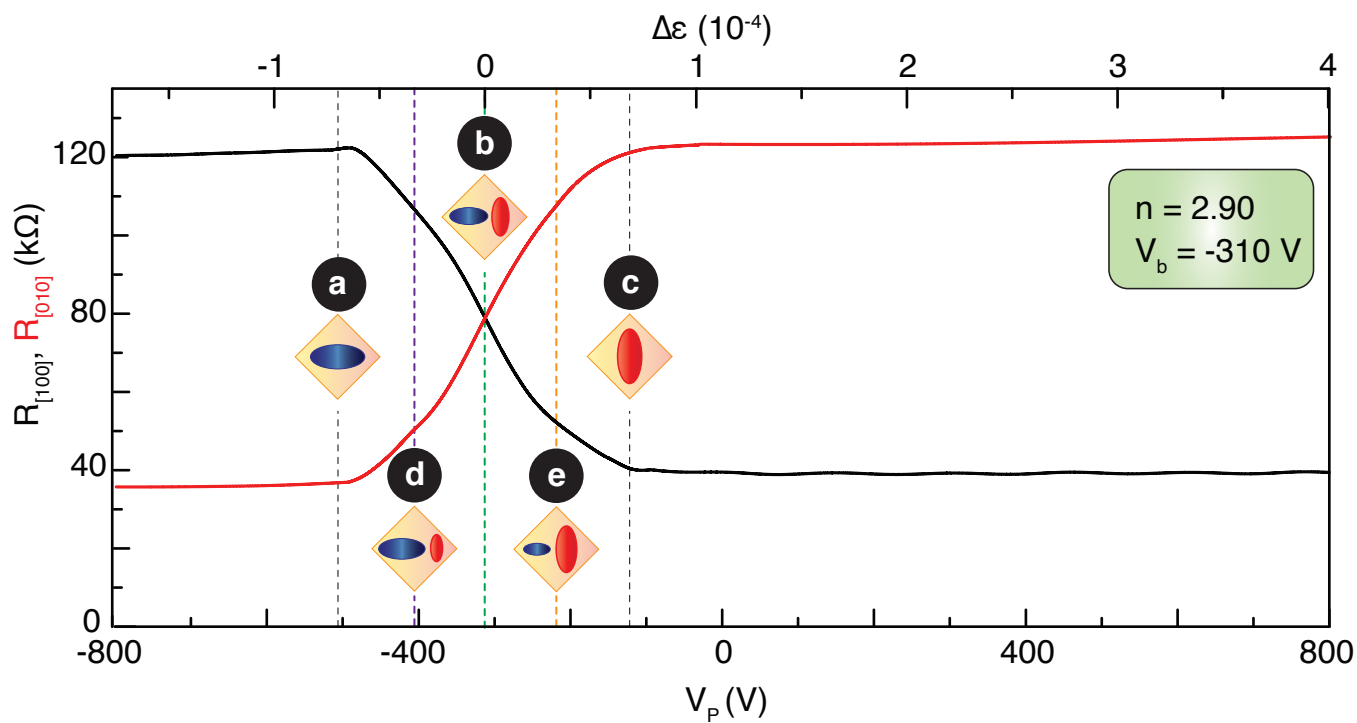


**Fig. S2.** Piezo-resistance of the sample at a density  $n = 2.90 \times 10^{10} \text{ cm}^{-2}$  as a function of piezo bias  $V_P$  and in-plane strain  $\Delta\varepsilon$  (top axis). Points **a - e** mark the valley occupation. The "balance" point, where the two ([100] and [010]) valleys are equally occupied, is achieved at a piezo bias of  $V_b = -310 \text{ V}$ . We can attain different valley occupancies by controlling  $V_P$ , i.e.  $\Delta\varepsilon$ .

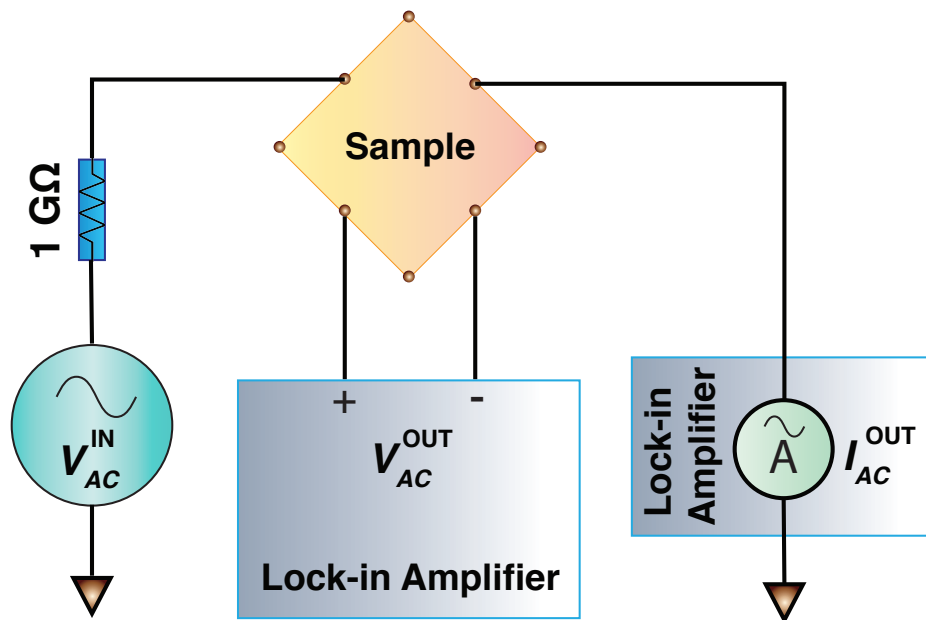
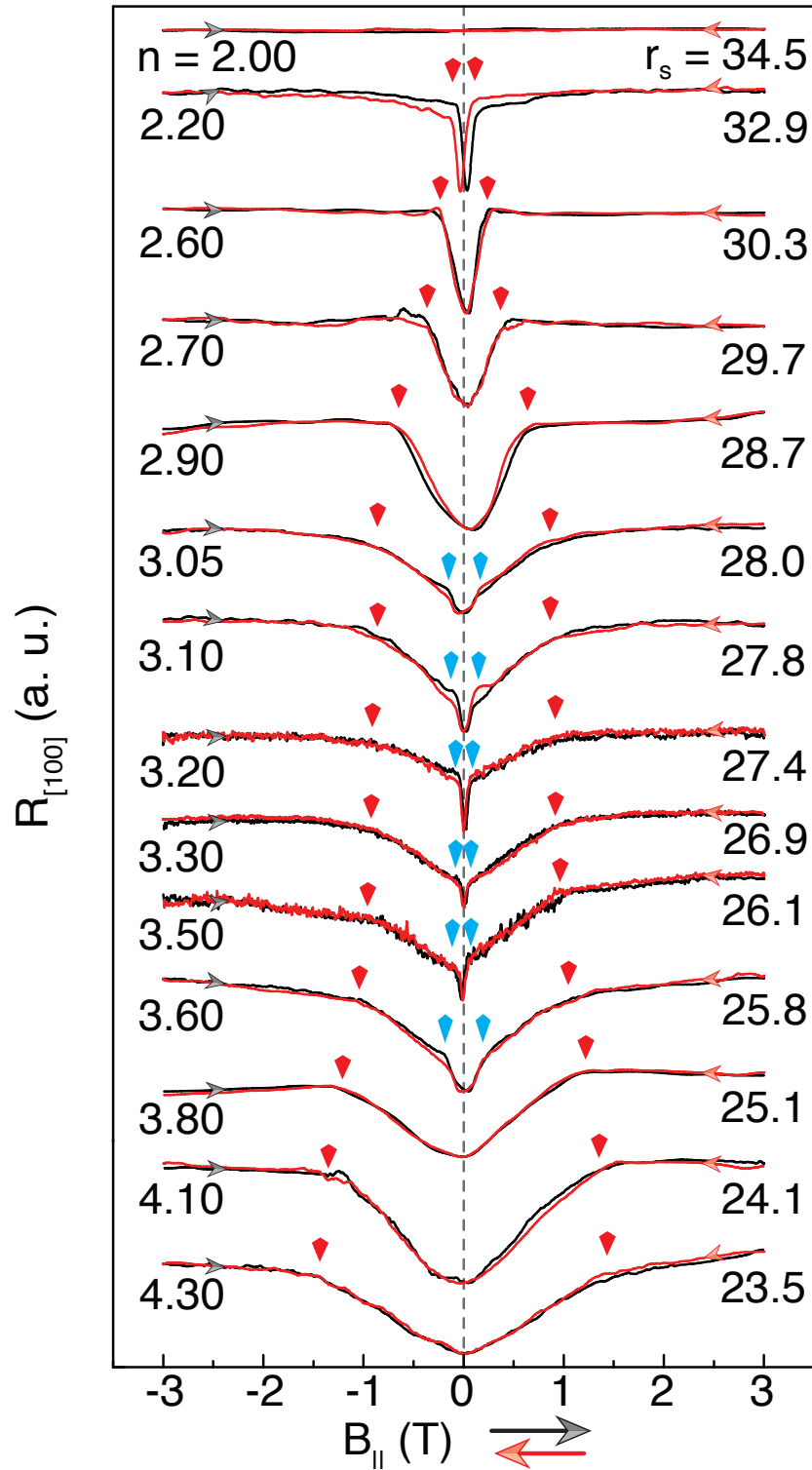
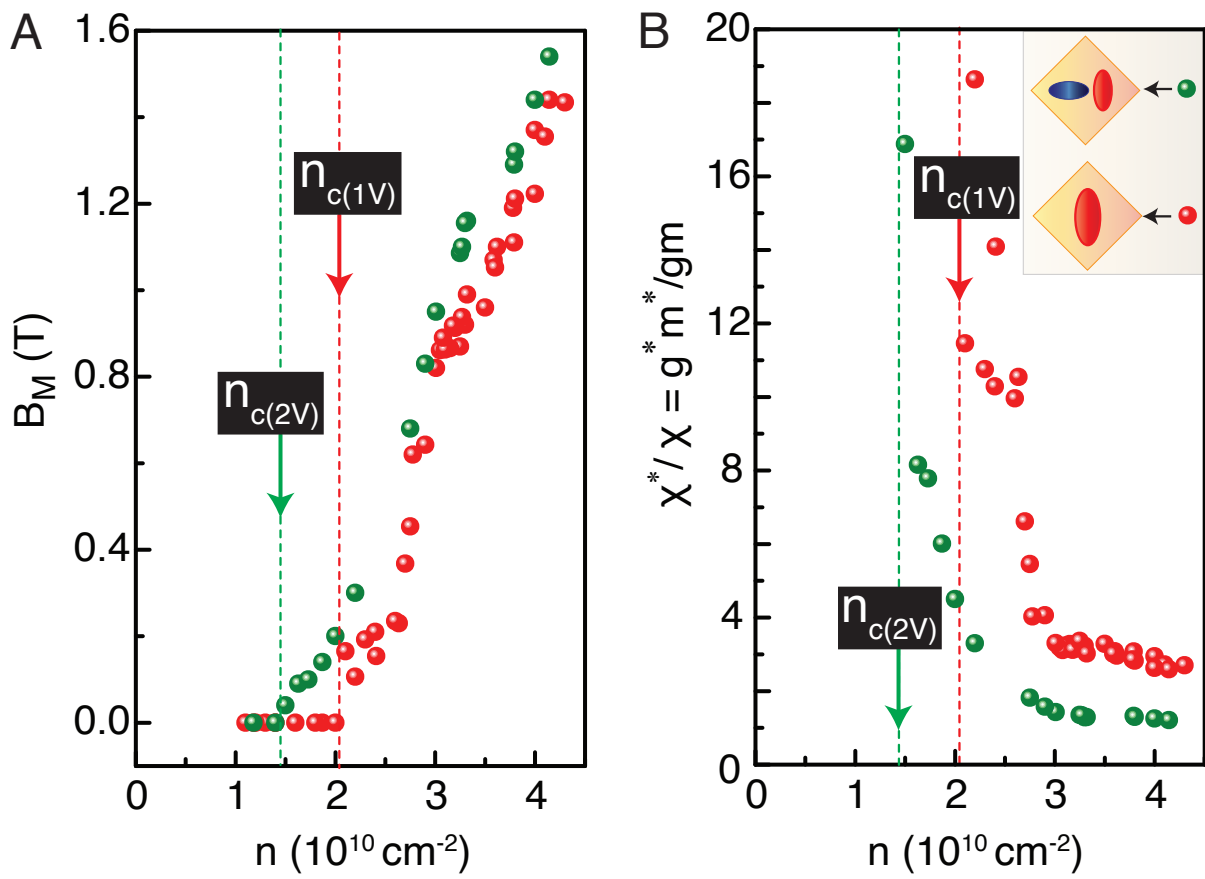


Fig. S3. Experimental setup showing the current injection and voltage probes used to measure  $V_{AC}$  and  $I_{AC}$  in order to obtain the sample resistance.





**Fig. S4.**  $R_{[100]}$  vs.  $B_{||}$  data taken at different 2DES densities. Traces are shown for both up- and down-sweeps of  $B_{||}$ , and are offset vertically for clarity. The vertical red arrows mark the positions of  $B_M$  above which the resistance saturates. In all the traces, the saturated value of magnetoresistance is almost twice the resistance at  $B = 0$ . In the density range  $3.0 \lesssim n \lesssim 3.6$ , the traces exhibit an additional feature at a very small  $B_{||}$  (marked with blue vertical arrows). When the 2DES density is tuned away from this density range, the extra feature disappears.



**Fig. S5.** Comparison of  $B_M$  and spin susceptibility for the single-valley and valley-degenerate 2DESSs, highlighting the difference in the critical density below which the system makes a ferromagnetic transition.

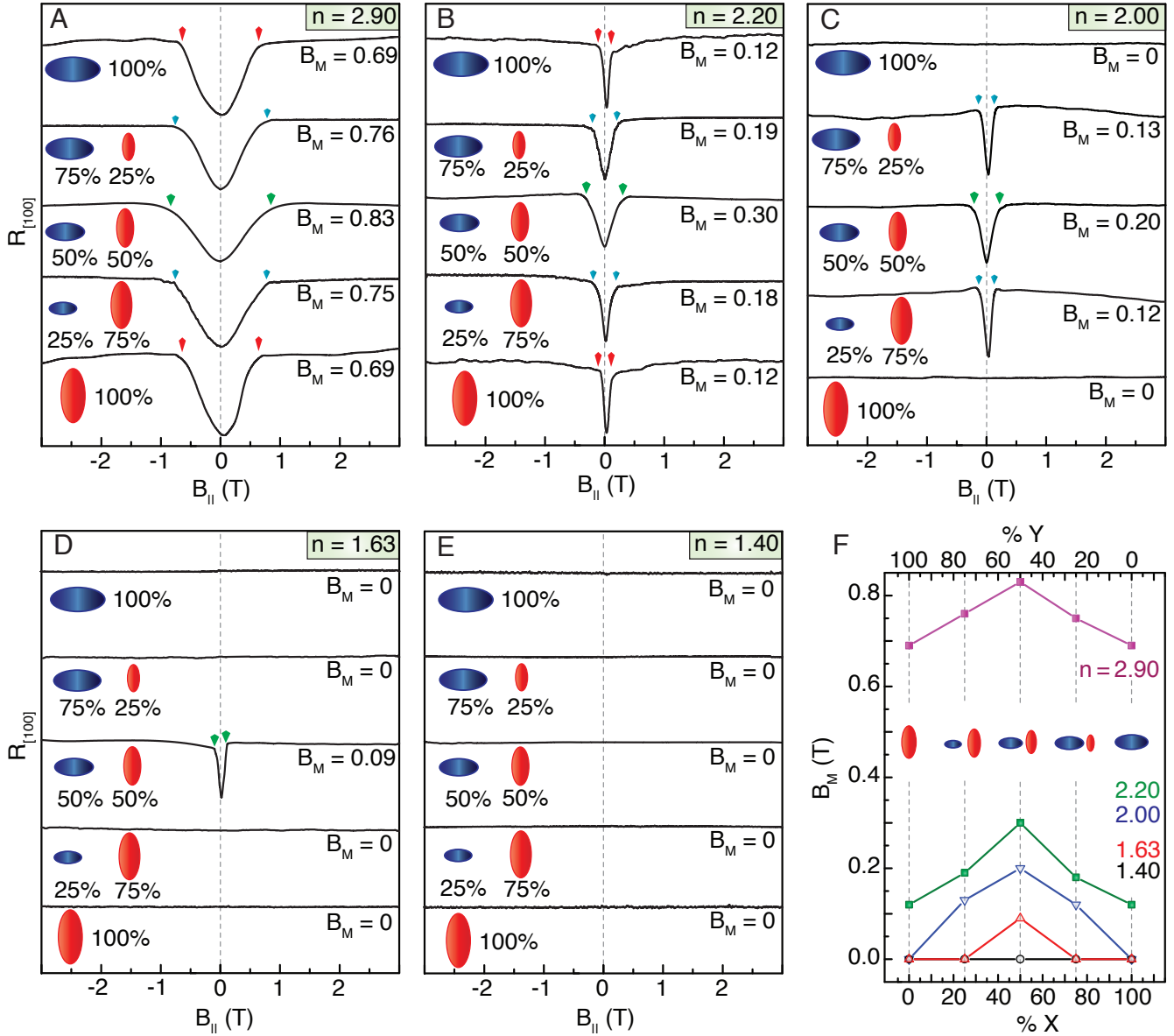


**Fig. S6.** Evolution of  $B_M$  as a function of valley occupancy. (A-E) Resistance vs. parallel magnetic field data taken at  $T = 0.30$  K for different 2DES densities demonstrating the effect of the valley occupancy on  $B_M$ . Traces are offset vertically. For each trace, the measured value of  $B_M$  is indicated (in units of T). At a fixed density, the 2DES has the smallest  $B_M$  when only one valley (either [100] or [010]) is occupied. As electrons start transferring from one valley to the other,  $B_M$  increases and reaches its maximum value when the valleys are equally occupied. The single-valley case reaches the ferromagnetic transition at the largest density while the valley-degenerate case requires the smallest density. (F)  $B_M$  plotted against the valley occupancy, summarizing the data in (A-E), and showing a clear increase in  $B_M$  as we move from a single-valley case towards the valley-degenerate case.

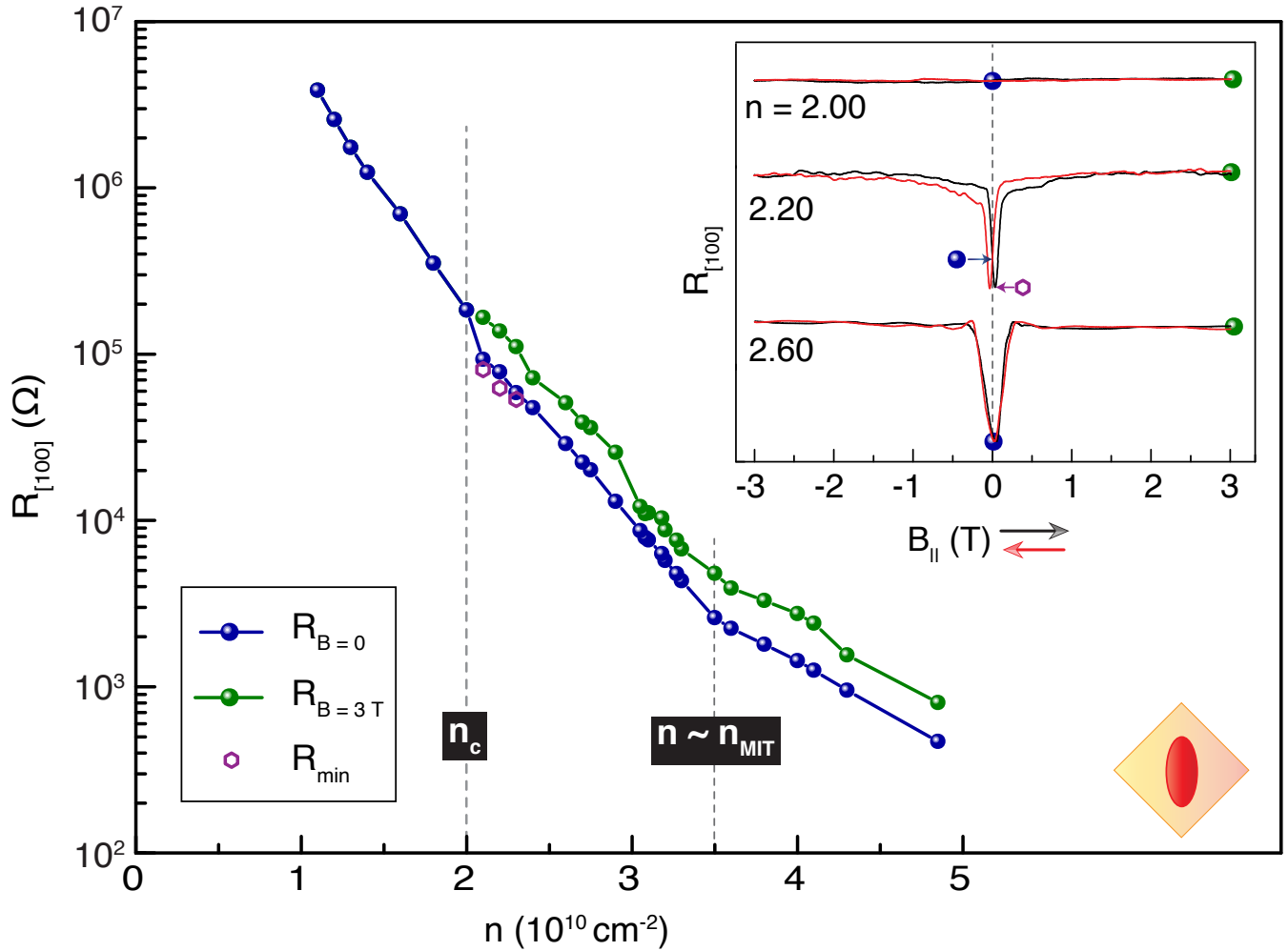


**Fig. S7.** Comparison between zero- and high-field values of sample resistance when the electrons are valley polarized. Plotted are the values of  $R_{[100]}$  at  $B_{||} = 0$  (blue circles) and 3T (green circles) as a function of electron density. Open purple symbols denote the resistance minima for the densities at which the minima are shifted from  $B = 0$  due to hysteresis. The inset illustrates the field locations of the data points. At  $n \leq 2.00$  (marked with a vertical line),  $R_{[100]}$  is independent of  $B_{||}$ , leading to an overlap between blue and green points. The zero-field resistance value at  $n = 2.00$  is very close to the high-field resistance value at  $n = 2.10$ , strongly suggesting that the 2DES is fully spin polarized at zero-field when  $n = 2.00$ , similar to the high-field case at  $n = 2.10$ . There is another sharp rise in resistance that happens near the MIT (at  $n = 3.5$ ), also marked with a dashed vertical line.

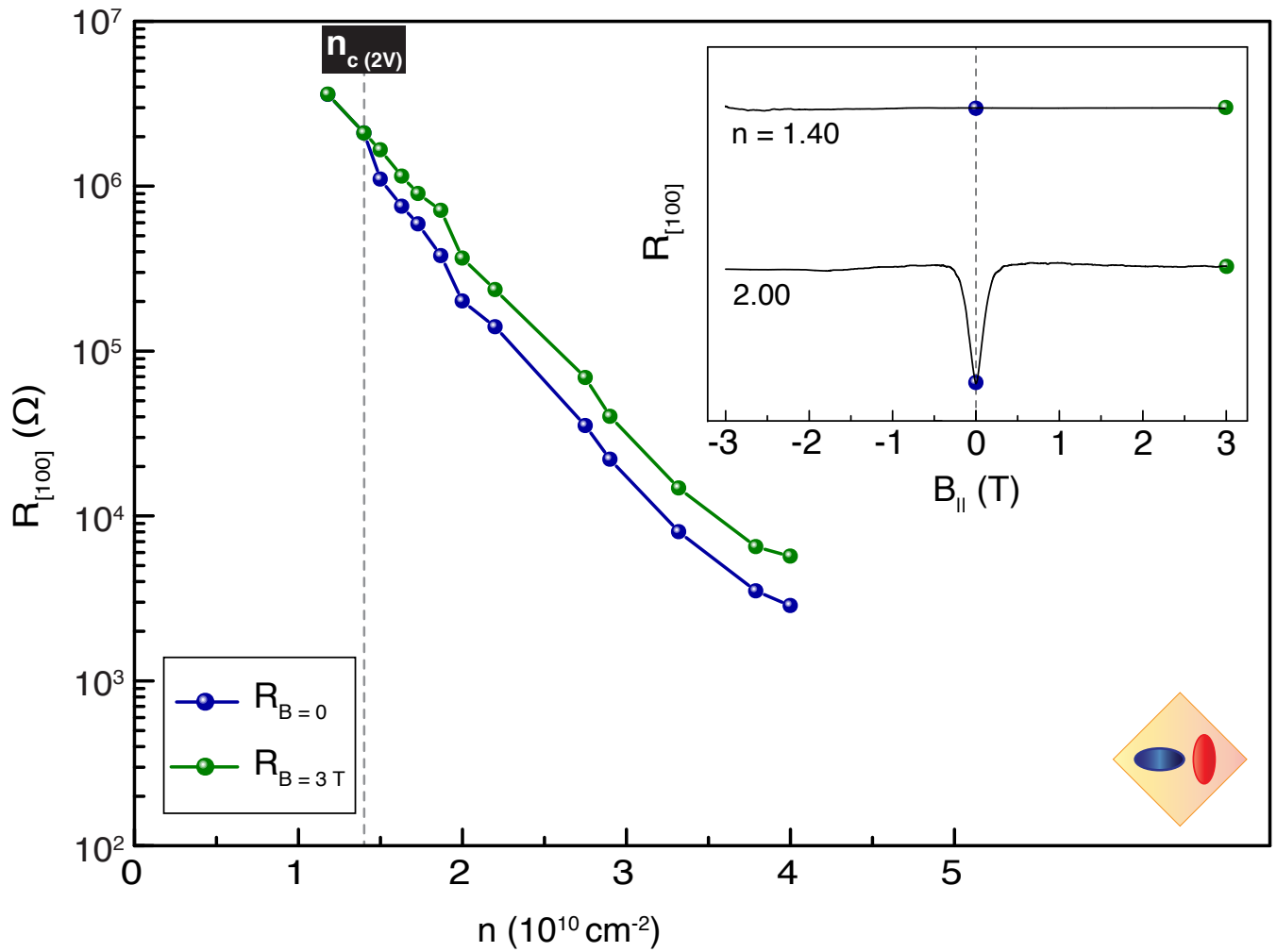


**Fig. S8.** Comparison between zero- and high-field values of sample resistance when the electrons occupy two degenerate valleys. Sample resistance,  $R_{[100]}$  is shown against electron density; blue and green circles represent the data points at  $B = 0$  and  $3T$ , respectively. The inset shows the field positions of the two types of points.  $R_{[100]}$  becomes independent of  $B_{||}$  when  $n \leq 1.40$  (marked with a vertical line), leading to an overlap between blue and green points. The zero-field resistance value at  $n = 1.40$  approaches the high-field resistance value at  $n = 1.50$ , supporting our conclusion of a full-spin-polarization transition at  $n = 1.40$  when the two valleys are degenerate.

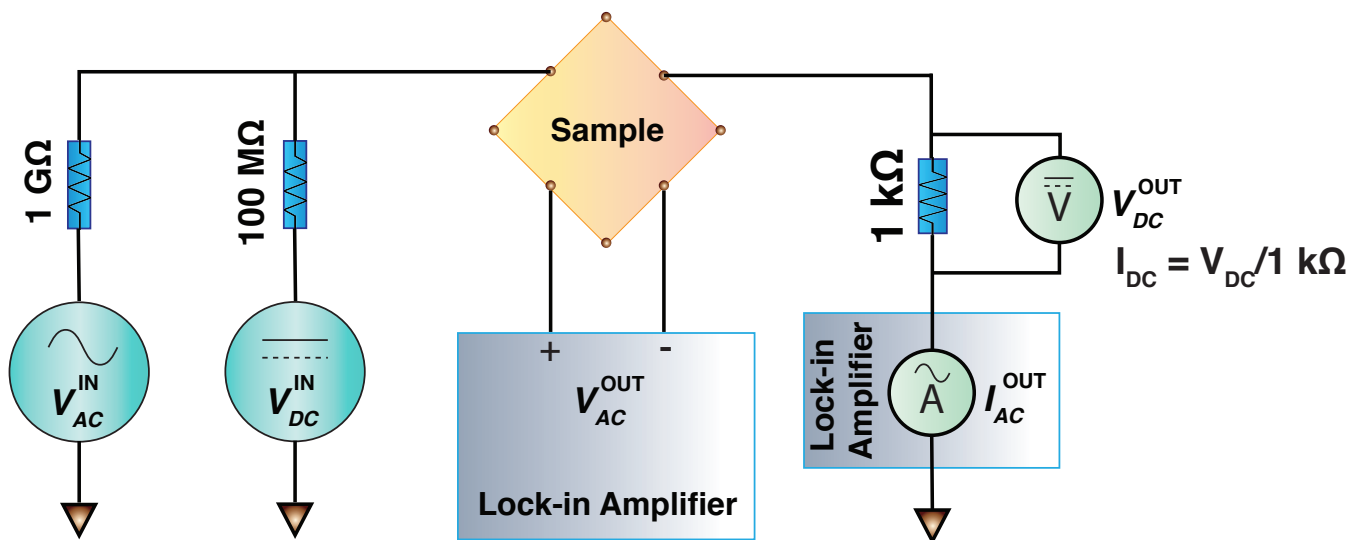
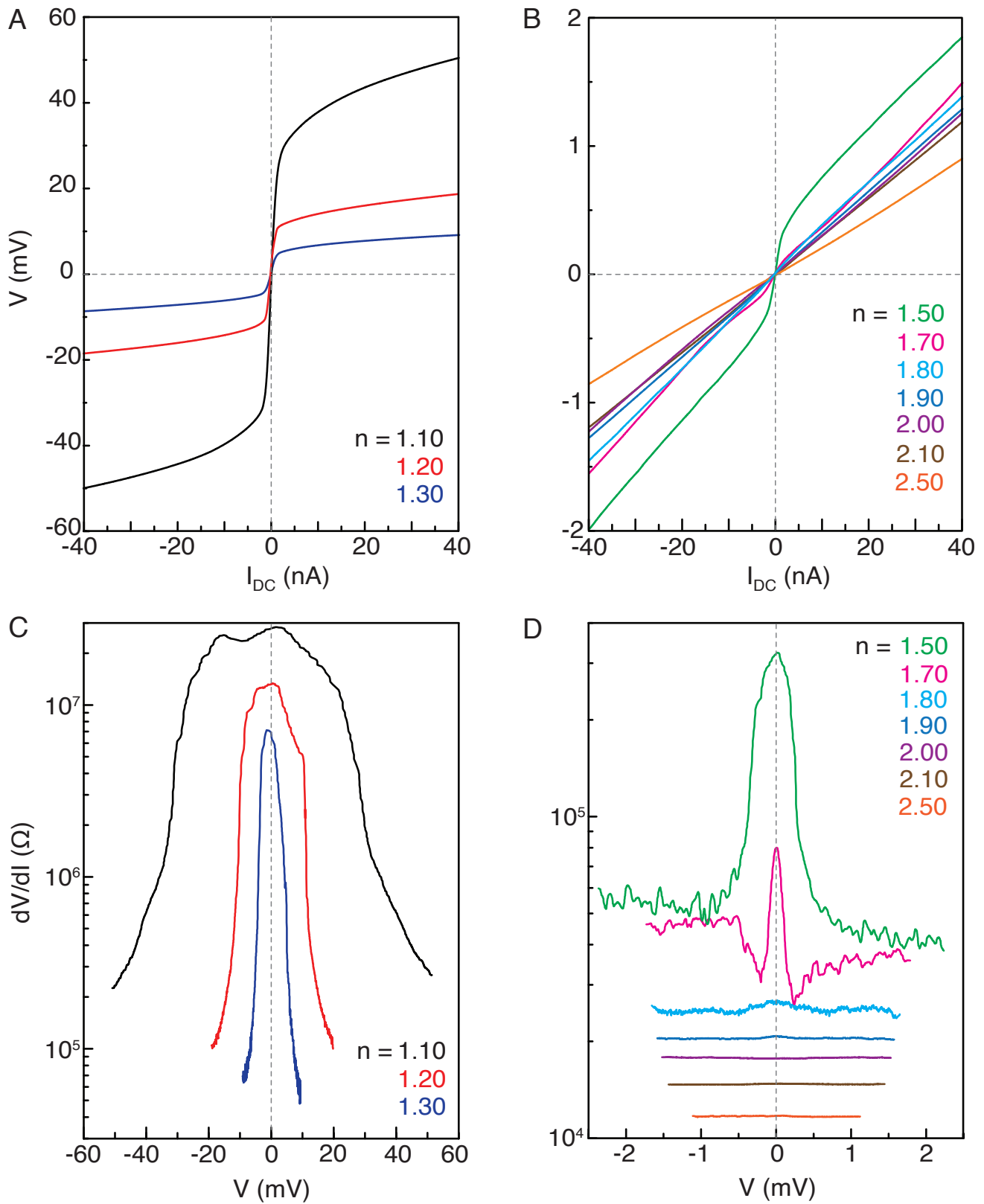
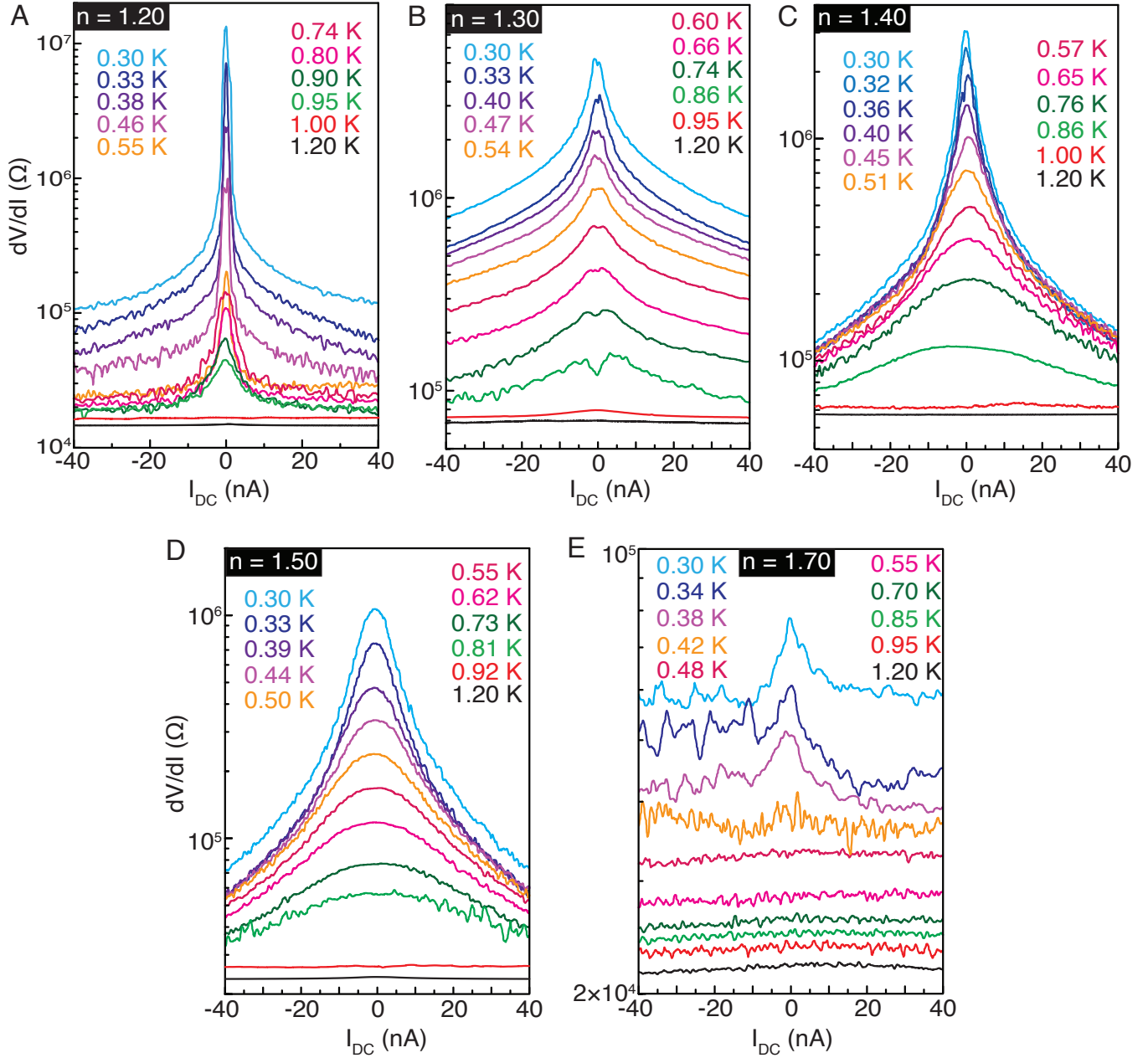


Fig. S9. Experimental setup for measuring differential resistance as a function of DC bias, showing the current injection and voltage leads used to measure both DC and AC quantities in order to obtain the  $dV/dI$  vs.  $I_{DC}$  plots.



**Fig. S10.** Density dependence of the non-linear  $I$ - $V$  characteristics at  $T = 0.30$  K. (A), (B)  $I$ - $V$  characteristics of the sample at different densities, exhibiting strong non-linearity at very low densities. (C), (D)  $dV/dI$  plotted against the voltage drop along the sample. The threshold voltage is very large (about 20 mV) at  $n = 1.10$ , and drops significantly (to a small fraction of 1 mV) as the density is raised to  $n = 1.70$  before the non-linearity disappears around  $n = 1.80$ . All the data are taken along the [100] direction, and only the [010] valley is occupied.



**Fig. S11.** Temperature dependence of  $dV/dI$  measured at densities (A)  $n = 1.20$ , (B)  $1.30$ , (C)  $1.40$ , (D)  $1.50$ , and (E)  $1.70$  along [010] direction, plotted against the DC bias current. All the electrons occupy the [010] valley. The temperature below which  $dV/dI$  shows non-linearity is smaller at higher densities, implying a reduction in the melting temperature of the Wigner solid.



223 **References**

- 224 1. E. P. De Poortere, Y. P. Shkolnikov, E. Tutuc, S. J. Papadakis, M. Shayegan, Enhanced electron mobility and high order  
225 fractional quantum Hall states in AlAs quantum wells. *Appl. Phys. Lett.* **80**, 1583 - 1585 (2002).
- 226 2. M. Shayegan, E. P. De Poortere, O. Gunawan, Y. P. Shkolnikov, E. Tutuc, K. Vakili, Two-dimensional electrons occupying  
227 multiple valleys in AlAs. *Phys. Stat. Sol. (b)* **243**, 3629 - 3642 (2006).
- 228 3. Y. J. Chung, K. A. Villegas Rosales, H. Deng, K. W. Baldwin, K. W. West, M. Shayegan, L. N. Pfeiffer, Multivalley  
229 two-dimensional electron system in an AlAs quantum well with mobility exceeding  $2 \times 10^6$  cm<sup>2</sup>/Vs. *Phys. Rev. Materials*  
230 **2**, 071001(R) (2018).
- 231 4. M. Shayegan, K. Karrai, Y. P. Shkolnikov, K. Vakili, E. P. De Poortere, S. Manus, Low-temperature, in situ tunable,  
232 uniaxial stress measurements in semiconductors using a piezoelectric actuator. *Appl. Phys. Lett.* **83**, 5235 - 5237 (2003).
- 233 5. Y. P. Shkolnikov, K. Vakili, E. P. De Poortere, M. Shayegan, Giant low-temperature piezoresistance effect in AlAs  
234 two-dimensional electrons. *Appl. Phys. Lett.* **85**, 3766 - 3768 (2004).
- 235 6. T. Gokmen, M. Padmanabhan, M. Shayegan, Transference of transport anisotropy to composite fermions. *Nat. Phys.* **6**,  
236 621 - 624 (2010).
- 237 7. O. Gunawan, Y. P. Shkolnikov, K. Vakili, T. Gokmen, E. P. De Poortere, M. Shayegan, Valley susceptibility of an  
238 interacting two-dimensional electron system. *Phys. Rev. Lett.* **97**, 186404 (2006).
- 239 8. Y. P. Shkolnikov, K. Vakili, E. P. De Poortere, M. Shayegan, Dependence of Spin Susceptibility of a Two-Dimensional  
240 Electron System on the Valley Degree of Freedom. *Phys. Rev. Lett.* **92**, 246804 (2004).
- 241 9. M. Padmanabhan, T. Gokmen, M. Shayegan, Enhancement of valley susceptibility upon complete spin polarization. *Phys.*  
242 *Rev. B* **78**, 161301(R) (2008).
- 243 10. T. Gokmen, M. Padmanabhan, M. Shayegan, Contrast between spin and valley degrees of freedom. *Phys. Rev. B* **81**,  
244 235305 (2010).
- 245 11. M. Marchi, S. D. Palo, S. Moroni, G. Senatore, Correlation Energy and the Spin Susceptibility of the Two-Valley  
246 Two-dimensional Electron Gas. *Phys. Rev. B* **80**, 035103 (2009).
- 247 12. N. D. Mermin, H. Wagner, Absence of Ferromagnetism or Antiferromagnetism in One- or Two-Dimensional Isotropic  
248 Heisenberg Models. *Phys. Rev. Lett.* **17**, 1133 - 1136 (1966).
- 249 13. J. Falson, Y. Kozuka, M. Uchida, J. H. Smet, T.-H. Arima, A. Tsukazaki, M. Kawasaki, MgZnO/ZnO heterostructures  
250 with electron mobility exceeding  $1 \times 10^6$  cm<sup>2</sup>/Vs. *Sci. Rep.* **6**, 26598 (2016).
- 251 14. J. Falson, M. Kawasaki, A review of the quantum Hall effects in MgZnO/ZnO heterostructures. *Rep. Prog. Phys.* **81**,  
252 056501 (2018).
- 253 15. J. G. Roch, G. Froehlicher, N. Leisgang, P. Makk, K. Watanabe, T. Taniguchi, R. J. Warburton, Spin-polarized electrons  
254 in monolayer MoS<sub>2</sub>. *Nat. Nanotechnol.* **14**, 432 - 436 (2019).
- 255 16. J. G. Roch, D. Miserev, G. Froehlicher, N. Leisgang, L. Sponfeldner, K. Watanabe, T. Taniguchi, J. Klinovaja, D. Loss, R.  
256 J. Warburton, First-order magnetic phase-transition of mobile electrons in monolayer MoS<sub>2</sub>. *Phys. Rev. Lett.* **124**, 187602  
257 (2020).
- 258 17. D. Miserev, J. Klinovaja, D. Loss, Exchange intervalley scattering and magnetic phase diagram of transition metal  
259 dichalcogenide monolayers. *Phys. Rev. B* **100**, 014428 (2019).
- 260 18. R. Pisoni, A. Kormányos, M. Brooks, Z. Lei, P. Back, M. Eich, H. Overweg, Y. Lee, P. Rickhaus, K. Watanabe, T.  
261 Taniguchi, A. Imamoglu, G. Burkard, T. Ihn, K. Ensslin, Interactions and Magnetotransport through Spin-Valley Coupled  
262 Landau Levels in Monolayer MoS<sub>2</sub>. *Phys. Rev. Lett.* **121**, 247701 (2018).
- 263 19. G. -B. Jo, Y. -R. Lee, J. -H. Choi, C. A. Christensen, T. H. Kim, J. H. Thywissen, D. E. Pritchard, W. Ketterle, Itinerant  
264 Ferromagnetism in a Fermi Gas of Ultracold Atoms. *Science* **325**, 1521 - 1524 (2009).
- 265 20. E. Vermeyen, C. A. R. Sá de Melo, J. Tempere, Exchange interactions and itinerant ferromagnetism in ultracold Fermi  
266 gases. *Phys. Rev. A* **98**, 023635 (2018).
- 267 21. Md. S. Hossain, T. Zhao, S. Pu, M. A. Mueed, M. K. Ma, K. A. V. Rosales, Y. J. Chung, L. N. Pfeiffer, K. W.  
268 West, K. W. Baldwin, J. K. Jain, M. Shayegan, Bloch ferromagnetism of composite fermions. *Nat. Phys.* (2020).  
269 <https://doi.org/10.1038/s41567-020-1000-z>
- 270 22. J. K. Jain, *Composite Fermions*. (Cambridge University Press, Cambridge, 2007).